

AD-A204 233

CHARACTERIZATION OF
MECHANICAL DAMAGE MECHANISMS
IN CERAMIC COMPOSITE MATERIALS

By
James Lankford, Jr.

TECHNICAL REPORT
ONR CONTRACT No. N00014-84-C-0213
ONR Contract Authority NR 032-553
SwRI-8124

For
Office of Naval Research
Arlington, VA 22217
By
Southwest Research Institute
San Antonio, Texas

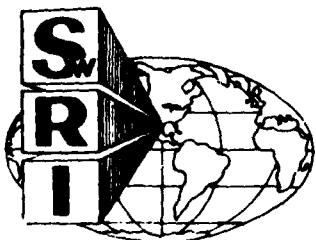
DTIC
ELECTED
FEB 02 1989
S D
S D

September 1988

Reproduction in whole or in part is permitted for any purpose of the United States Government

DISTRIBUTION STATEMENT A

Approved for public release
Distribution Unlimited



SOUTHWEST RESEARCH INSTITUTE
SAN ANTONIO

HOUSTON

88 11 17 004

SOUTHWEST RESEARCH INSTITUTE
Post Office Drawer 28510, 6220 Culebra Road
San Antonio, Texas 78284

CHARACTERIZATION OF MECHANICAL DAMAGE MECHANISMS IN CERAMIC COMPOSITE MATERIALS

By
James Lankford, Jr.

TECHNICAL REPORT
ONR CONTRACT No. N00014-84-C-0213
ONR Contract Authority NR 032-553
SwRI-8124

For
Office of Naval Research
Arlington, VA 22217

By
Southwest Research Institute
San Antonio, Texas

September 1988

Reproduction in whole or in part is permitted for any purpose of the United States Government

Approved:



Gerald R. Leverant, Director
Department of Materials Sciences

UNCLASSIFIED

SECURITY CLASSIFICATION OF THIS PAGE

AD-H-24-233

Form Approved
OMB No 0704-0188
Exp Date Jun 30 1986

REPORT DOCUMENTATION PAGE

1a. REPORT SECURITY CLASSIFICATION Unclassified		1b. RESTRICTIVE MARKINGS	
2a. SECURITY CLASSIFICATION AUTHORITY		3. DISTRIBUTION/AVAILABILITY OF REPORT DTIC USERS Limited	
2b. DECLASSIFICATION/DOWNGRADING SCHEDULE		4. PERFORMING ORGANIZATION REPORT NUMBER(S) S-8124	
5. MONITORING ORGANIZATION REPORT NUMBER(S) NR 032-553		6a. NAME OF PERFORMING ORGANIZATION Southwest Research Institute	
6b. OFFICE SYMBOL (if applicable)		7a. NAME OF MONITORING ORGANIZATION Dr. Steven G. Fishman - Code 431N Office of Naval Research	
6c. ADDRESS (City, State, and ZIP Code) 6220 Culebra Road, P.O. Drawer 28510 San Antonio, TX 78284		7b. ADDRESS (City, State, and ZIP Code) 800 North Quincy Street Arlington, VA 22217	
8a. NAME OF FUNDING/SPONSORING ORGANIZATION Office of Naval Research		8b. OFFICE SYMBOL (if applicable)	
8c. ADDRESS (City, State, and ZIP Code) 800 North Quincy Street Arlington, VA 22217		9. PROCUREMENT INSTRUMENT IDENTIFICATION NUMBER N00014-84-C-0123	
		10. SOURCE OF FUNDING NUMBERS	
		PROGRAM ELEMENT NO.	PROJECT NO.
		TASK NO.	WORK UNIT ACCESSION NO.
11. TITLE (Include Security Classification) Characterization of Mechanical Damage Mechanisms in Ceramic Composite Materials			
12. PERSONAL AUTHOR(S) James Lankford			
13a. TYPE OF REPORT Technical		13b. TIME COVERED FROM 05/23/87 TO 05/24/88	
14. DATE OF REPORT (Year, Month, Day) September 1988		15. PAGE COUNT	
16. SUPPLEMENTARY NOTATION <i>fr. back</i>			
17. COSATI CODES		18. SUBJECT TERMS (Continue on reverse if necessary and identify by block number) Key Words: compressive strength; partially stabilized zirconia; temperature effects; composite materials; fracture mechanisms; ceramics; plastic flow; glass matrix ceramics;	
19. ABSTRACT (Continue on reverse if necessary and identify by block number) High-strain rate compressive failure mechanisms in fiber-reinforced ceramic matrix composite materials have been characterized. These are contrasted with composite damage development at low-strain rates, and with the dynamic failure of monolithic ceramics. It is shown that it is possible to derive major strain-rate strengthening benefits if a major fraction of the fiber reinforcement is aligned with the load axis. This effect considerably exceeds the inertial microfracture strengthening observed in monolithic ceramics, and non-aligned composites. Its basis is shown to be the trans-specimen propagation time period for heterogeneously-nucleated, high-strain kink bands.			
A brief study on zirconia has focussed on the remarkable inverse strength-strain rate result previously observed for both fully and partially-stabilized zirconia single crystals, whereby the strength <u>decreased</u> with increasing strain rate. Based on the (continued)			
20. DISTRIBUTION/AVAILABILITY OF ABSTRACT <input checked="" type="checkbox"/> UNCLASSIFIED/UNLIMITED <input type="checkbox"/> SAME AS RPT. <input type="checkbox"/> DTIC USERS		21. ABSTRACT SECURITY CLASSIFICATION Unclassified	
22a. NAME OF RESPONSIBLE INDIVIDUAL James Lankford		22b. TELEPHONE (Include Area Code) 512/522-2317	
22c. OFFICE SYMBOL			

UNCLASSIFIED

SECURITY CLASSIFICATION OF THIS PAGE

19. hypothesis that the suppression of microplastic flow, hence, local stress relaxation, might be responsible for this behavior, fully stabilized (i.e., non-transformable) specimens were strain-gaged and subjected to compressive microstrain. The rather stunning observation was that the crystals are highly microplastic, exhibiting plastic yield on loading, and anelasticity and reverse plasticity upon unloading. These results clearly support the hypothesis that with increasing strain rate, microcracking is favored at the expense of microplasticity. *Keywords.*

4
FLD 18

UNCLASSIFIED

FOREWORD

This report describes recent work carried out under an experimental program aimed at characterizing damage mechanisms and compressive failure in ceramic-matrix composite materials. The report consists of two papers, each having been submitted to the journal noted on its title page.



Accession For	
NTIS	CRA&I <input checked="" type="checkbox"/>
DTIC	TAB <input type="checkbox"/>
Unannounced <input type="checkbox"/>	
Justification	
By <i>per ltr</i>	
Distribution/	
Availability Codes	
Dist	Avail and/or Special
A-1	

TABLE OF CONTENTS

	<u>Page</u>
LIST OF ILLUSTRATIONS.....	iv
I. DYNAMIC COMPRESSIVE FRACTURE IN FIBER-REINFORCED CERAMIC MATRIX COMPOSITES.....	1
Abstract.....	1
Introduction.....	1
Experimental Approach.....	4
Results.....	5
Discussion.....	9
Conclusions.....	26
Acknowledgment.....	26
References.....	27
II. INVERSE STRAIN RATE EFFECTS AND MICROPLASTICITY IN ZIRCONIA CRYSTALS.....	28
Acknowledgments.....	35
References.....	35

LIST OF ILLUSTRATIONS

		Page
FIGURES		
I.	DYNAMIC COMPRESSIVE FRACTURE IN FIBER-REINFORCED CERAMIC MATRIX COMPOSITES	
1	Compressive Strength Versus Strain Rate for Several Monolithic Ceramics at 23°C.....	3
2	Schematic of Sleeved HPB Configuration to Permit Specimen Damage Without Failure.....	6
3	Compressive Strength Versus Strain Rate for SiC Fiber-Reinforced Pyroceram.....	7
4	Compressive Strength Versus Strain Rate for Pyroceram.....	8
5	Deformation Mechanisms in Pyroceram; T = 1100°C, $\dot{\epsilon} = 10^{-5}\text{ s}^{-1}$	10
6	Kink band crossing several 0/90 plies; stress axis vertical, T = 800°C, $\dot{\epsilon} \approx 2 \times 10^3\text{ s}^{-1}$	11
7	Kink band in 0/90 composite, showing shear displacement d versus shear gage length l_0 ; $\dot{\epsilon} = 10^3\text{ s}^{-1}$, stress axis vertical.....	12
8	Kink band in 0/90 composite, showing microfragmentation of matrix to accommodate SiC fiber fracture and rotation; T = 23°C, $\dot{\epsilon} = 2 \times 10^3\text{ s}^{-1}$, stress axis vertical.....	13
9	Magnified view of region A in Figure 8, showing (arrows) possible adiabatic viscous flow in matrix material and SiC fiber; note blunt crack tips in latter, apparent local necking in former.....	14
10	Section through 90° ply in 0/90 composite, showing non-center-to-center interfiber microfracture; T = 23°C, $\dot{\epsilon} = 0.6 \times 10^3\text{ sec}^{-1}$ stress axis vertical.....	16
11	Schematic of Matrix Microfracture Associated with Off-Axis Fibers.....	17

LIST OF ILLUSTRATIONS (cont'd)

	Page
12 Schematic of Kink Band Propagation Over a Macroscopic Dimension &	19
13 Experimental Versus Theoretical (Static Plus Kink Propagation) Dynamic Strength for 0° Composite.....	22
14 Extrapolation of Composite and Pyroceramic Dynamic Strengths to $\dot{\epsilon} = 10^5 \text{ s}^{-1}$, Compared with Theoretical Ultimate Strength.....	23
15 Schematic Representation of Damage-Strain Rate Regimes in Ceramics and Fiber-Reinforced Ceramic Matrix Composites.....	25
 II. INVERSE STRAIN RATE EFFECTS AND MICROPLASTICITY IN ZIRCONIA CRYSTALS	
1 Compressive Strength Versus Strain Rate for Zirconia Single Crystals.....	31
2 Stress-Microstrain During Compressive Load-Unload.....	33

DYNAMIC COMPRESSIVE FRACTURE IN FIBER-REINFORCED
CERAMIC MATRIX COMPOSITES

I.

James Lankford
Department of Materials Sciences
Southwest Research Institute
San Antonio, TX

ABSTRACT

High-strain rate compressive failure mechanisms in fiber-reinforced ceramic matrix composite materials have been characterized. These are contrasted with composite damage development at low-strain rates, and with the dynamic failure of monolithic ceramics. It is shown that it is possible to derive major strain-rate strengthening benefits if a major fraction of the fiber reinforcement is aligned with the load axis. This effect considerably exceeds the inertial microfracture strengthening observed in monolithic ceramics, and non-aligned composites. Its basis is shown to be the trans-specimen propagation time period for heterogeneously-nucleated, high-strain kink bands.

I. Introduction

It is by now well known that brittle materials subjected to high rates of loading often exhibit strengths much greater than those characteristic of slow or quasistatic rates [1-5]. The degree of strengthening observed is generally too high, and too strain-rate sensitive, to be explained on the basis of the suppression of thermally activated crack tip processes, although the latter does impart a mild rate-dependent strength benefit [1]. For example, the author has shown that for strain rates $\geq 10^3 \text{ s}^{-1}$, obtainable within the split

Hopkinson pressure bar (HPB), certain classes of monolithic ceramics (Figure 1) behave according to [1]

$$\sigma_c \propto \dot{\epsilon}^n \quad (1)$$

where σ_c is the compressive failure (fracture) strength, $\dot{\epsilon}$ is the imposed strain rate, and n is a constant, usually of the order of 1/3. Others have obtained similar results for rocks, in both compression and tension [2-7]. Where this behavior has not been observed (Figure 1), fracture mode/micro-structural considerations ($\text{RB Si}_3\text{N}_4$), or strain-rate limitations inherent in the HPB (Al_2O_3), are thought to be responsible.

In fact, it has been shown by Grady and Lipkin [8] that analyses based on a variety of physical criteria (work of fracture, least action law, inertia of flaws to crack initiation, crack inertia under step loading) all lead inevitably to a tensile fracture relationship like Equation (1), i.e.,

$$\sigma_T \propto \dot{\epsilon}^{1/3} \quad (2)$$

where σ_T is the applied tensile stress at failure. Since brittle compressive failure is known to correspond to the coalescence of a multitude of microscopic cracks nucleated within local tensile regions, it is therefore not surprising that equivalent failure dynamics should obtain for both tension and compression. Generalizing the situation, Grady and Kipp observe [8] that such results suggest that a cube-root strain-rate dependence represents the upper limit that can be obtained in the dynamic brittle failure process. This probably is true for monolithic materials, but recent experimental results [9] seem to indicate that the microstructures of ceramic matrix composites can be manipulated to yield a much higher degree of strain-rate sensitivity.

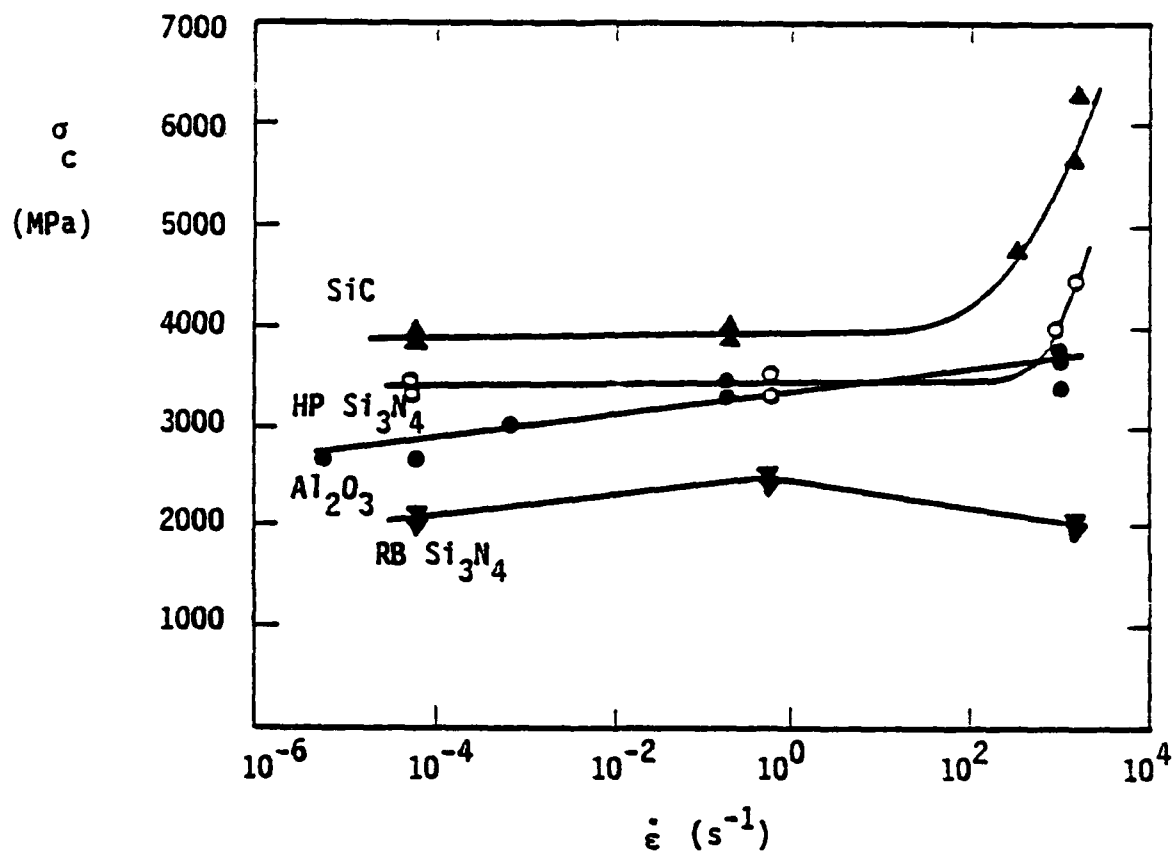


Figure 1. Compressive Strength Versus Strain Rate for Several Monolithic Ceramics at 23°C. The decrease in strength for reaction bonded (RB) Si_3N_4 at $\dot{\epsilon} \approx 10^3 s^{-1}$ is caused by a transition in fracture mode from transgranular to intergranular.

The objective of the present paper is to briefly outline these results, and then establish the principal factors which appear to control the damage development/failure process. A simple basis for treating the problem analytically is presented.

II. Experimental Approach

The materials studied have been described in detail elsewhere [9,10], and so are discussed here only briefly. Thus, the composites* consisted essentially of a pyroceramic matrix reinforced with about 46% of 15 μm diameter SiC fibers laid up in two variants. In the first (0° variant), the fibers were oriented unidirectionally, and compression specimen axes were aligned with the fibers. For the second variant, fibers were laid up in 200 μm thick planar bundles, with the fibers in alternating layers at 90° to one another. Specimen axes in this case were either parallel to one set of fibers (0/90), or lay at 45° to both sets (45/45). The matrix, which also was tested, was a polycrystalline lithium-alumina-silicate with grains ranging in size from 0.5-2.0 μm . Further microstructural details for both matrix and composite are discussed elsewhere [9-12].

Cylindrical compression specimens (10 mm long by 5 mm in diameter) were machined from the as-received composite panels and from the monolithic ceramic matrix bodies. Specimens were tested in air at temperatures ranging from 23°C to 1100°C, over a strain range of 10^{-4}s^{-1} to $> 10^3\text{s}^{-1}$. The latter dynamic rates were obtained by means of a split HPB apparatus. Nickel-base superalloy rings were honed so as to just fit the ends of each composite specimen, to prevent failure by brooming.

* Compglas®, United Technologies Research Center

Damage introduced during dynamic loading (low-strain rate damage has been discussed elsewhere [10]) was characterized by optical and scanning electron microscopy of impacted but unfailed specimens. This state was achieved by enclosing the latter within slightly shorter high-strength steel sleeves (Figure 2). Prior to failure, the composites "flow" as damage accumulates [9,10]; this process can be arrested at any desired strain level by carefully adjusting sleeve lengths to absorb the load at the appropriate point on the stress-strain curve. The intact, but deformed, specimens thereby obtained can then be sectioned and polished for study.

III. Results

As shown in Figure 3, the strength of the composite material is relatively strain-rate independent for $\dot{\epsilon} \leq 10^2 \text{ s}^{-1}$, above which the strength of 0° and 0/90 variants obey

$$\sigma_c \propto \dot{\epsilon}^{-0.77} \quad (3)$$

while for the 45/45 material

$$\sigma_c \propto \dot{\epsilon}^{-0.3} \quad (4)$$

It should be observed that the relative strength ordering at low strain rates is preserved within the high-rate regime, and that the strength decrement between 0° and 0/90 variants is essentially constant, i.e., $\Delta\sigma_c \approx 350 \text{ MPa}$.

For the matrix material alone (Figure 4), σ_c versus $\dot{\epsilon}$ is basically constant for temperatures $\leq 800^\circ\text{C}$ until $\dot{\epsilon} \approx 10^3 \text{ s}^{-1}$, above which Equation 4 again holds. Although the strength is quite strain rate sensitive at 1100°C ,

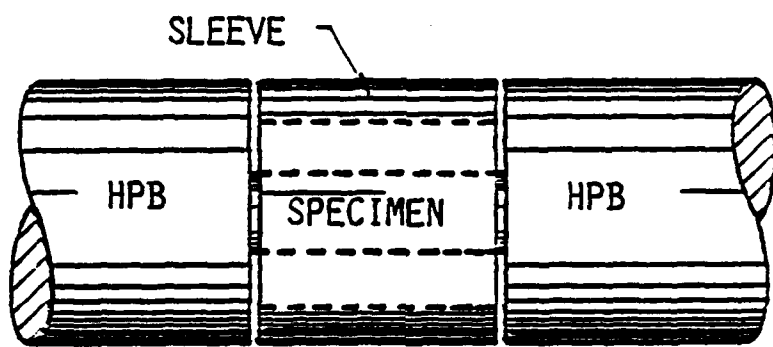


Figure 2. Schematic of Sleeved HPB Configuration to Permit Specimen Damage Without Failure.

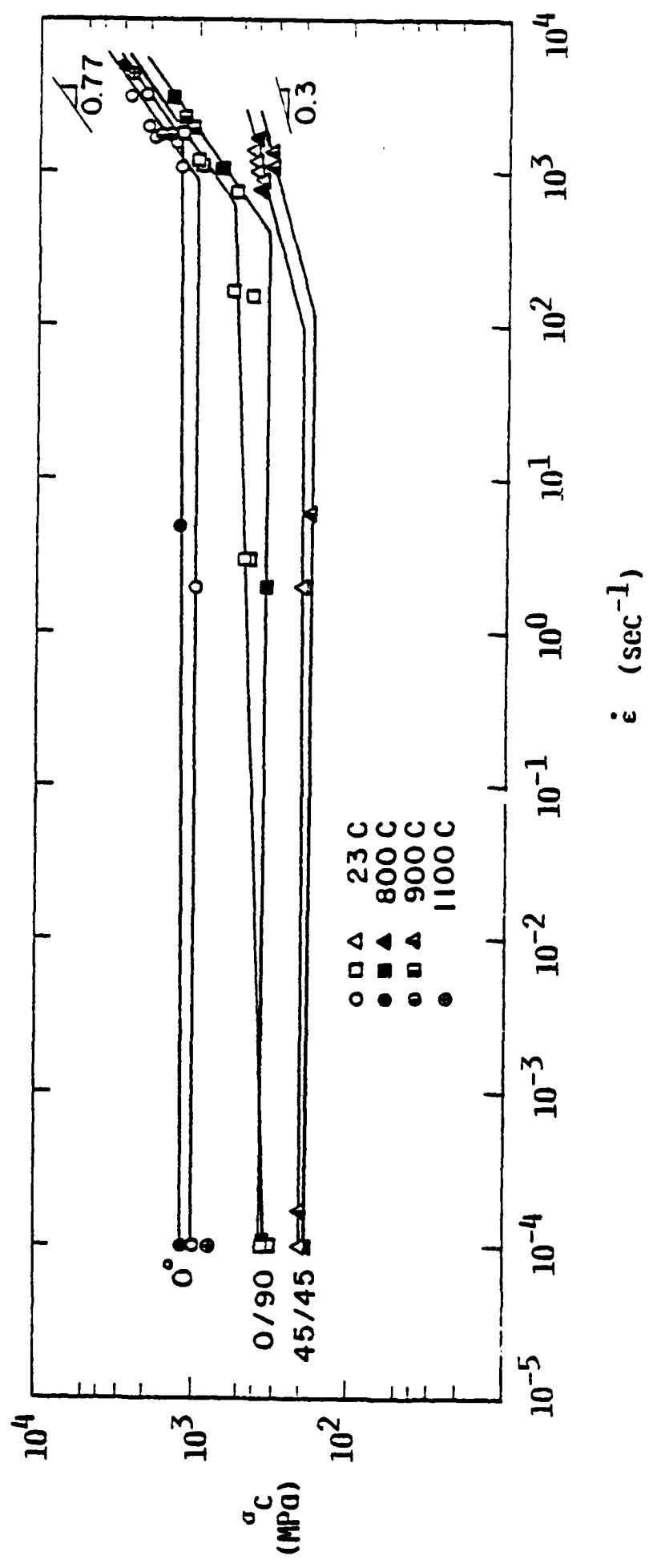


Figure 3. Compressive Strength Versus Strain Rate for SiC Fiber-Reinforced Pyroceram.

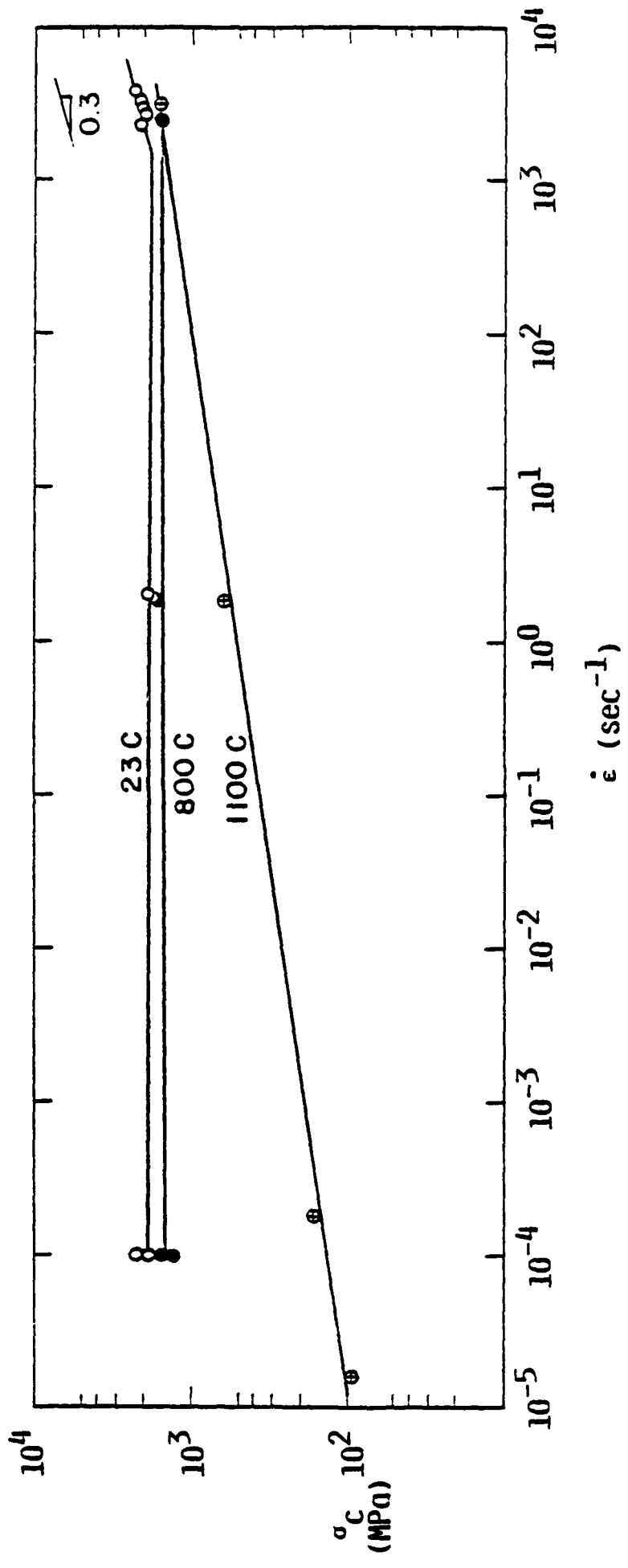


Figure 4. Compressive Strength Versus Strain Rate for Pyroceram.

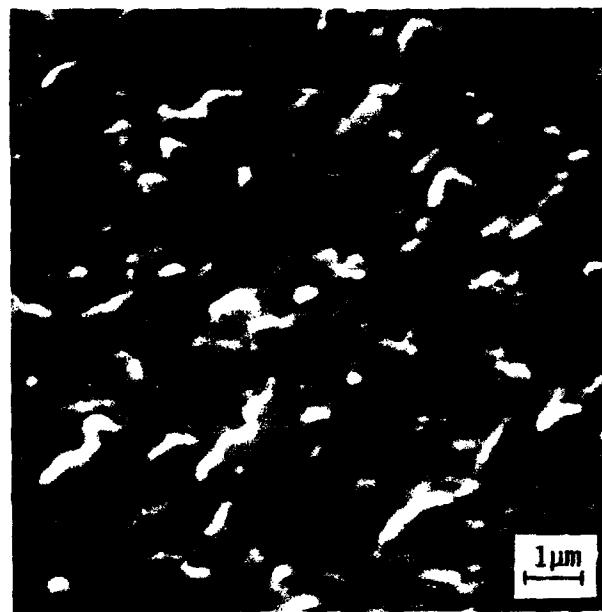
it is interesting to note that at high strain rates, the thermally activated failure process (grain boundary sliding and cavitation, Figure 5) is defeated. Within this strain rate regime, pyroceram failure is catastrophic at all temperatures, and brought about by the rapid coalescence of a multitude of microcracks.

It was shown in an earlier paper [10] that at low-strain rates, the composite material fails in compression by matrix microfracture, which accommodates a general fiber buckling process followed by gross failure via localized fiber kinking. This is not what happens at high-loading rates. Sections of damaged, but unfailed, sleeved 0° and 0/90 HPB specimens reveal no buckling, but instead (Figure 6) a number of isolated, but macroscopic, shear bands. At least one end (usually both ends) of each such band is associated with a vertical microfracture zone (arrow, Figure 6); the latter appears to accommodate the intense shear within a given band. Formation of the shear zones occurs at all temperatures studied. Behavior of the 45/45 composite differed in that it simply disintegrated catastrophically, similar to the matrix material itself.

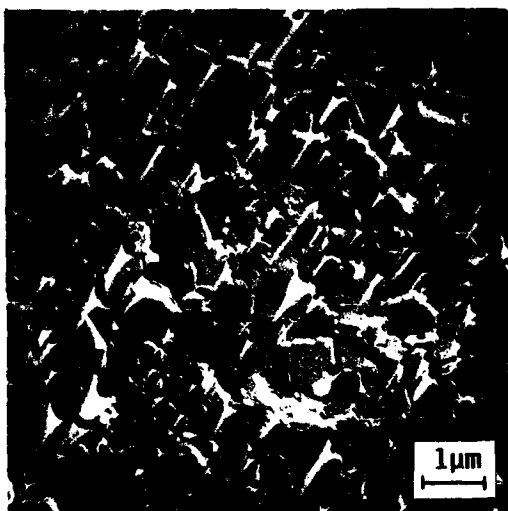
Comparing d and ξ_0 in Figure 7, it is evident that kink band shear strains (d/ξ_0) can easily exceed unity. These are accomplished by the propagation of kinks in SiC fibers (Figure 8), accompanied by local microfracture and/or matrix flow (arrows, Fig. 9); the latter would require near adiabatic heating. Work is in progress to permit discrimination between these two possibilities.

IV. Discussion

The fact that the strengths of the monolithic matrix and the 45/45 composite increase as $\dot{\epsilon}^{-0.3}$ at high-loading rates, and that both fail via



(a) SEM showing grain boundary sliding



(b) TEM surface replica showing cavitation
(black dots) caused by grain boundary
sliding

Figure 5. Deformation mechanisms in pyroceram; $T = 1100^\circ\text{C}$,
 $\dot{\epsilon} = 10^{-5}\text{s}^{-1}$.



Figure 6. Kink band crossing several 0/90 plies;
stress axis vertical, $T = 800^\circ\text{C}$,
 $\dot{\epsilon} \approx 2 \times 10^3 \text{ s}^{-1}$. Arrow indicates zone of
microfracture within 90° ply at end of
band.



Figure 7. Kink band in 0/90 composite, showing shear displacement d versus shear gage length l_0 ;
 $\dot{\epsilon} = 10^3 \text{ s}^{-1}$, stress axis vertical.

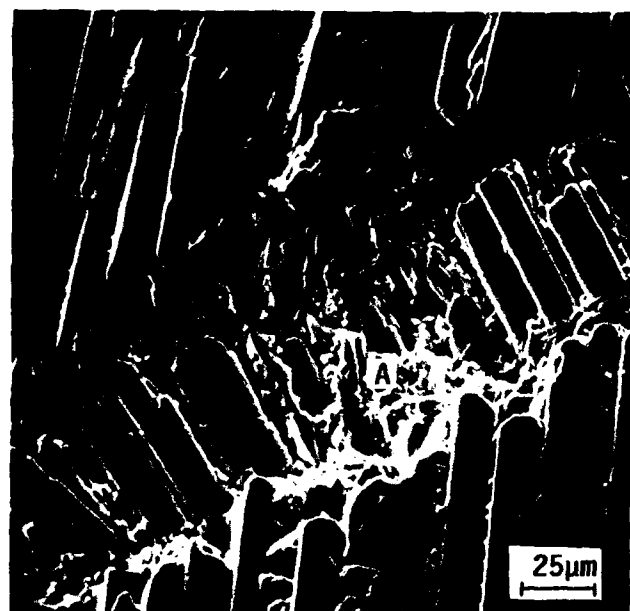


Figure 8. Kink band in 0/90 composite, showing
microfragmentation of matrix to accommodate
SiC fiber fracture and rotation; $T = 23^\circ\text{C}$,
 $\dot{\epsilon} = 2 \times 10^3 \text{s}^{-1}$, stress axis vertical.



Figure 9. Magnified view of region A in Figure 8, showing (arrows) possible adiabatic viscous flow in matrix material and SiC fiber; note blunt crack tips in latter, apparent local necking in former.

rapid microcrack coalescence, suggests that inertia-controlled, homogeneous microfracture is responsible for failure. This also suggests that the presence of fibers at other than 0° provides a weakening effect which probably derives from their role as "microanvils," fracturing the matrix at a significantly lower stress than that which obtains in the pure matrix. It can be shown that this is likely by considering analytically the idealized case of the 0/90 material, in which the 90° fibers form perfect hardness indenters.

Study of sections through such specimens show (Figure 10) that cracks form between individual fibers as sketched in Figure 11a, i.e., they follow an arced, non-centerline path. This is reminiscent of the behavior of cone cracks beneath a blunt punch, suggesting that the situation might be idealized as shown in Fig. 11b. In the vicinity of a round, flat indenter, the maximum tensile stress (which nucleates cone cracks) is approximately

$$\sigma_T^{\max} \approx \frac{P}{\pi a^2} \left(\frac{1-v}{2}\right) \quad (5)$$

where P is the applied load, a is the area of contact, and v is Poisson's ratio. If $a \approx R/2$ (when R is the fiber radius), and $v = 0.25$, then

$$\sigma_T^{\max} \approx 4\sigma(.375) \quad (6)$$

where σ is the applied compressive stress. Earlier work [1,13] has shown that microcracking can be monitored by acoustic emission, which for 0/90 composites begins when $\sigma \approx 270$ MPa [13]. From Equation (6), this means $\sigma_T^{\max} \approx 400$ MPa when interfiber matrix microcracking begins, which correlates with the experimentally measured matrix tensile strength, 430 MPa.

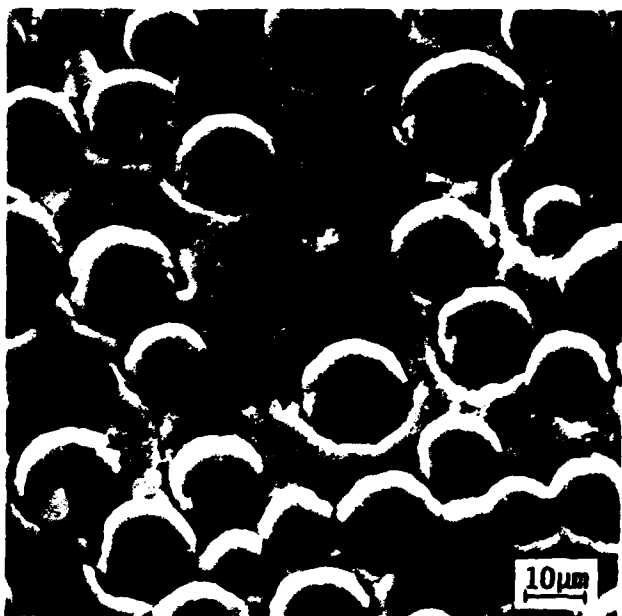
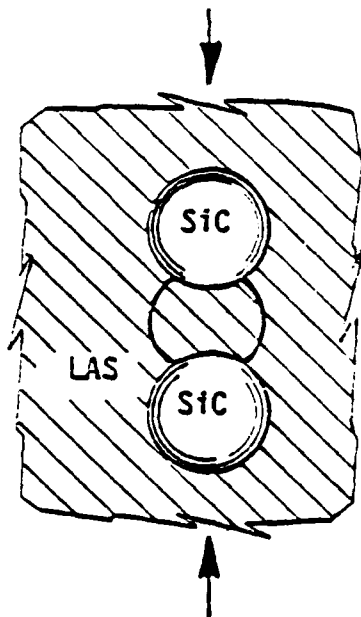
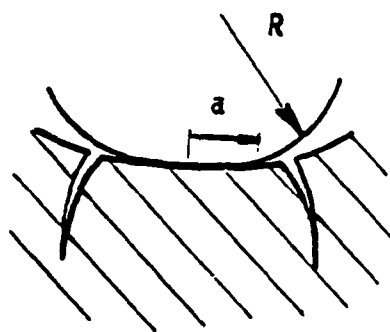


Figure 10. Section through 90° ply in 0/90 composite,
showing non-center-to-center interfiber
microfracture; $T = 23^\circ\text{C}$, $\dot{\epsilon} \approx 0.6 \times 10^3 \text{ sec}^{-1}$
stress axis vertical.



(a) Non-center-to-center fracture
between adjacent fibers



(b) Representation of fiber-matrix
interaction as punch-cone crack
problem

Figure 11. Schematic of Matrix Microfracture Associated with Off-Axis Fibers.

The presence of such effective crack initiators in 0/90 material evidently accounts for the persistent difference in strength between 0° and 0/90 composites over the entire strain-rate regime. Further, since the difference exists at high loading rates, tensile microfracture inertia must be included within the observed strain-rate sensitivity for both 0° and 0/90 layups. However, the high strain rate specimens actually fail by shear fault nucleation and propagation; the latter can be shown to contribute an additional, significant rate-dependent term.

Specifically, in the most general case, the strain rate at failure is given by

$$\dot{\epsilon} = \frac{\dot{\sigma}_f}{E} = \frac{\sigma_f}{Et_f} \quad (7)$$

where $\dot{\sigma}_f$ is the compressive stress rate, σ_f is the compressive failure stress, and E is the elastic modulus. If failure corresponds only to the propagation of a narrow shear fault, or kink band ($\sigma_f = \sigma_k$), by a characteristic macroscopic dimension ℓ (Figure 12), then

$$t_f \approx \ell/c_s \quad (8)$$

where c_s is the shear velocity. Eliminating t_f yields

$$\sigma_k \approx \left(\frac{E\ell}{c_s} \right) \dot{\epsilon} \quad (9)$$

hence

$$\sigma_k \propto \dot{\epsilon}^{1.0} \quad (10)$$

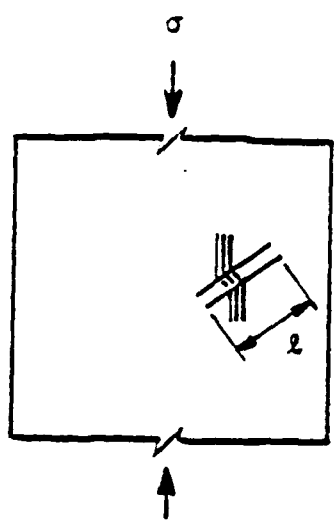


Figure 12. Schematic of Kink Band Propagation Over a Macroscopic Dimension l .

It should be appreciated that this process cannot take place without local accommodation of the initial 0°-kink responsible for shear band formation. Evans and Adler [14], for example, have analyzed the micromechanics of kinking in three-dimensional composites capable of at least some plastic flow. Consideration of their result, which includes a variety of microstructural and material parameters, indicates that the compressive strength depends mainly on the matrix yield strength. In the present instance, the matrix clearly does not yield, but can fragment via local tensile microfracture, and thereby produce a shear instability capable of accommodating a kink by the sliding/rotation of the fragments.

Such accommodation appears to be responsible for the off-fault plane microfracture attending the ends of the present kink bands (Figure 6). Since the kink cannot form until the matrix "yields," it is likely that local tensile microfracture precedes dynamic kink formation. This is in accord with the earlier suggestions that a differing microfracture threshold is responsible for the observed constant (strain rate-independent) difference between 0° and 0/90 compressive strengths.

Accommodation by local microfracture would imply, of course, a cube root strain-rate contribution to the composite dynamic compressive strength, in addition to the first power factor (Equation 9) derived for kink propagation. Unfortunately, it is not as straight-forward to produce an equivalent expression for the inertial microcrack term, since modeling to date has dealt only with tensile external loading. For example, for impulsive tensile loading of a penny-shaped crack, Kipp, et al. [15] have shown that

$$\sigma_f = \left(\frac{9\pi E K^2 I_c}{16 N^2 c_s} \right)^{1/3} \dot{\epsilon}^{1/3} \quad (11)$$

where K_{Ic} is the fracture toughness, and N is a crack geometry term. However, while the same strain rate dependence should obtain for compressive loading, the correct form of coefficient for compression is unknown. That is, the magnitude of the failure stress must reflect the resolution of an applied compressive field into local tensile enclaves due to factors such as geometric flaws (pores, microcracks), intrinsic flaws (twins, dislocations), and elastic compliance mismatch across grain boundaries. Since no such analogue to Equation 11 is available, the accommodation (via inertial microcracking) contribution to the dynamic kink process cannot be estimated directly.

Accordingly, the composite compressive strength under impulsive loading can be written as

$$\sigma_c = \sigma_0 + \left(\frac{E\dot{\epsilon}}{c_s}\right) \dot{\epsilon} + A \left(\frac{9\pi E K_{Ic}^2}{16 N c_s}\right)^{1/3} \dot{\epsilon}^{1/3} \quad (12)$$

where σ_0 represents the approximately constant, thermally activated, quasistatic compressive strength, and A is a constant greater than unity representing the resolution (compressive to tensile) and amplification of the applied stress during kink accommodation. For present purposes, let us consider the case of the 0° composite, for which $\sigma_0 \approx 950$ MPa, $E = 131$ GPa, $c_s = 7.24 \times 10^3$ m/s, and $\dot{\epsilon}$ is assumed to be approximately 8.5 mm. Figure 13 compares experimental results (average for $T = 23^\circ\text{C}$ to 1100°C) with the first two terms in Equation 12. Agreement seems reasonable, especially considering that if A were known, inclusion of the inertial kink accommodation term would shift the theoretical curve upward, closer to the experimental results.

It is interesting to compare the behavior of the composite material with its monolithic ceramic matrix, as shown in Figure 14. Although the former is weaker than the latter for strain rates less than $\sim 10^3 \text{s}^{-1}$, the situation is

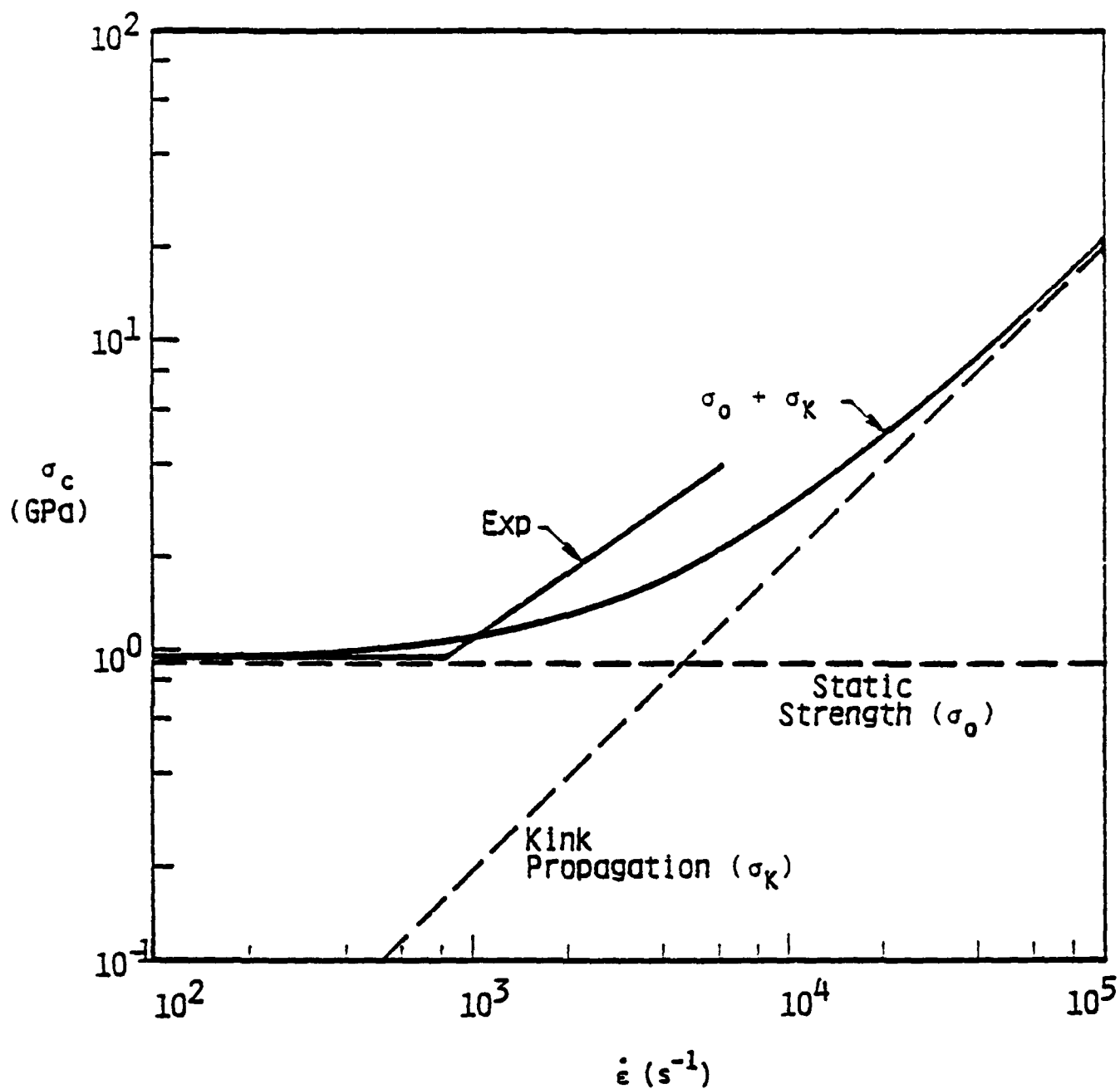


Figure 13. Experimental Versus Theoretical (Static Plus Kink Propagation) Dynamic Strength for 0° Composite. Addition of inertial kink accommodation term would raise the theoretical curve.

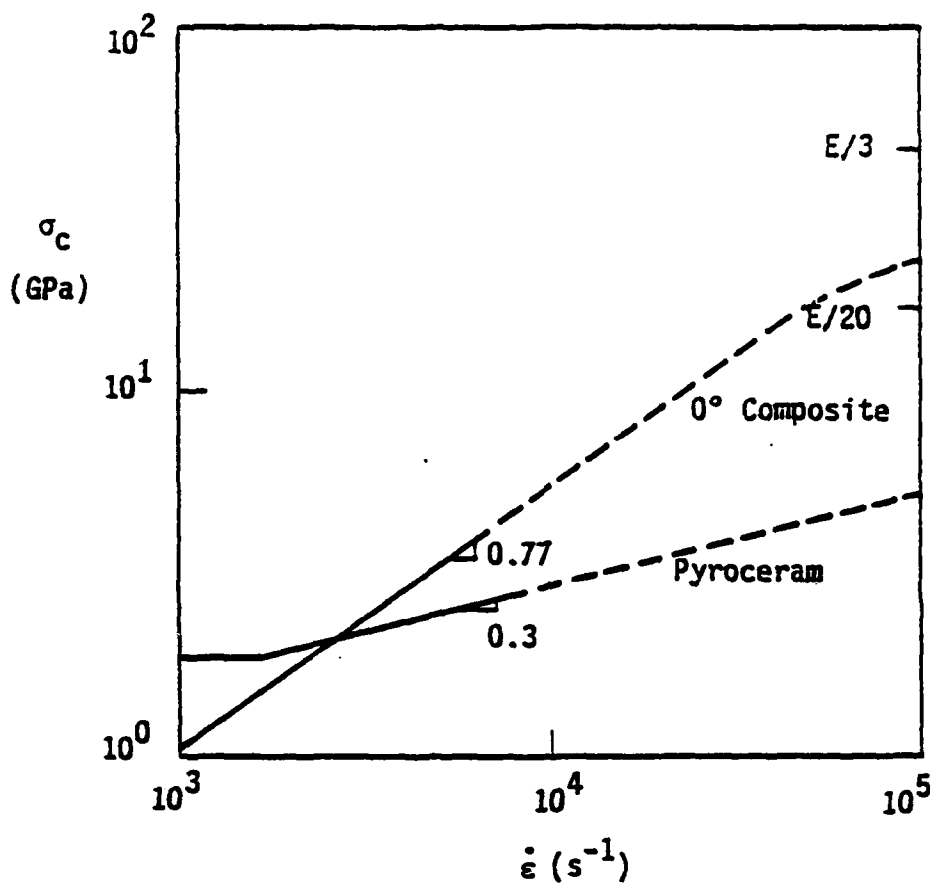


Figure 14. Extrapolation of Composite and Pyroceramic Dynamic Strengths to $\dot{\epsilon} = 10^5 s^{-1}$, Compared with Theoretical Ultimate Strength.

reversed once the powerful strain-rate strengthening of the composite begins to dominate the inertial (cube root) rate hardening of the monolithic material. Extrapolation of this effect, which is a direct result of the time-dependent complexity of the composite failure process, predicts that the reinforced material will achieve its maximum theoretical strength ($E/20$ to $E/3$) at the relatively modest strain rate of $\sim 10^5 \text{ s}^{-1}$, while the pyroceram will not reach the same value until $\dot{\epsilon} = 10^8 \text{ s}^{-1}$. This result clearly has interesting implications for practical situations (armor, shock loading). In addition, it is relevant to wonder whether similar complexity in failure, with its associated strain-rate strengthening might be engendered via high aspect ratio whisker, versus continuous fiber, reinforcement. That is, it seems likely that composites containing a fairly high density of such fibers, preferentially oriented and extensively overlapping, would also experience kink nucleation and propagation during dynamic loading/failure.

Finally, it should be noted that the macroscopic dynamic strain rates used to correlate the present results do not represent the true state of affairs obtaining within the local kink bands. While macroscopic strains at failure were on the order of 0.01, it will be recalled that strains within discrete shear bands were on the order of 1.0. Accordingly, actual strain rates within these regions must have been well in excess of 10^5 s^{-1} ; it therefore would not be surprising for the flow process within such a fast deformation field to be adiabatic. This would be in accord with some of the viscous-like features noted within the kink bands (i.e., Figure 9), and would suggest that matrix flow was beginning to compete with microfracture.

Factors involved in the strain-rate dependence of fiber reinforced, ceramic matrix composites are summarized schematically in Figure 15. While the thermally activated and plastic flow plateaus are relatively flat, the

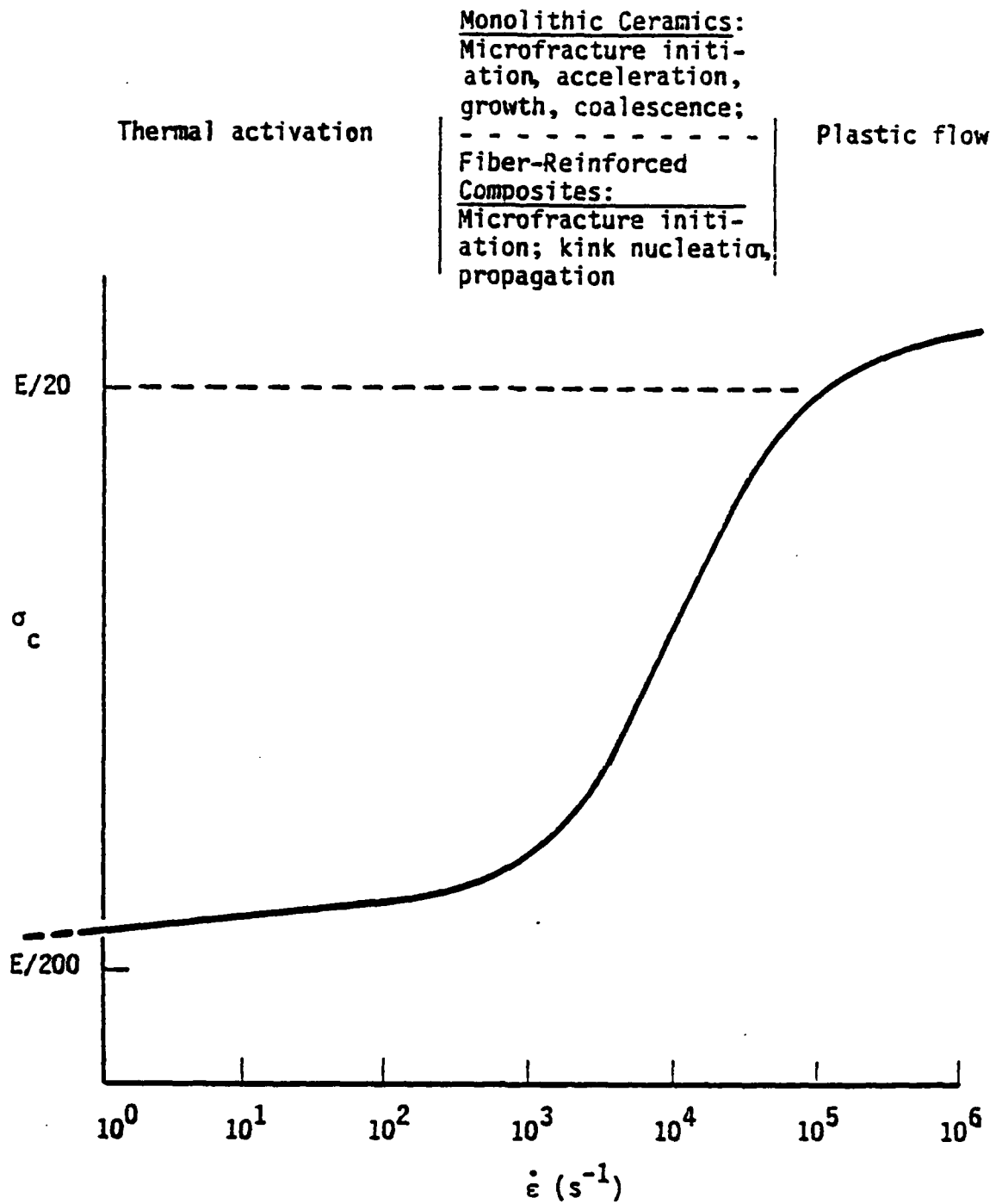


Figure 15. Schematic Representation of Damage-Strain Rate Regimes in Ceramics and Fiber-Reinforced Ceramic Matrix Composites.

transition regime $10^2 \text{ s}^{-1} \leq \dot{\epsilon} \leq 10^6 \text{ s}^{-1}$ is extremely strain rate sensitive. Both the strain rate hardening within, and the threshold (minimum $\dot{\epsilon}$) for, this regime are amenable to optimization by means of composite microstructural modification.

V. Conclusions

It has been shown that compressive strain-rate hardening well in excess of the cube root theoretical maximum for brittle materials can be achieved, if the failure mechanism can be made sufficiently complex. In particular, fiber reinforcement in the direction of the compression axis necessitates a combined failure mode involving inertia-controlled microcrack accommodation of heterogeneous kink band nucleation, followed by rate dependent kink propagation. The latter involves very high local strain rates, so high, in fact, that local heating may be involved in the shear process. The results suggest that a high density of preferentially-oriented, high aspect-ratio whiskers might provide similar strain-rate strengthening benefits.

Acknowledgment

The support of the Office of Naval Research through Contract No. N00014-84-C-0213 is gratefully acknowledged. In addition, the author appreciates the careful experimental work of Mr. A. Nicholls, and the kind provision of Compglas material by Dr. C. Prewo of United Technologies Research Center.

REFERENCES

1. J. Lankford, Fracture Mechanics of Ceramics, 5 (1983) 625-637.
2. D.E. Grady and R.E. Hollenbach, Geophys. Res. Letters, 6, (1979) 76-76.
3. D.E. Grady and M.E. Kipp, Int. J. Rock Mech. Min. Sci., in press, 1979.
4. S.J. Green and R.D. Perkins, K.E. Gray (ed.), Proceedings of 10th Symposium on Rock Mechanics, American Institute of Mining, Metallurgical, and Petroleum Engineers, Austin, 1968.
5. J. Lankford, Journal of the American Ceramic Society, 65 [18] (1982) C-122.
6. D.L. Birkimer, K.E. Gray (ed.), Proceedings 12th Symposium on Rock Mechanics, American Institute of Mining, Metallurgical, and Petroleum Engineering, Austin, 1971.
7. M.J. Forrestal, D.E. Grady, and K.W. Schuler, Int. J. Rock Mech. Min. Sci., 15 (1978) 263-265.
8. D.E. Grady and J. Lipkin, Geophys. Res. Lttrs. 7 (1980) 255.
9. J. Lankford, Composites, 18 [2] (1987) 145-152.
10. J. Lankford, W.C. Harrigan (ed.), J. Strife (ed.), and A.K. Dhingra (ed.), Proceedings of the Fifth International Conference on Composite Materials (ICCMV), TMS-AIME, Warrendale, 1985.
11. K.M. Prewo, ONR Technical Report, Contract No. N00014-81-C-0571, 1983.
12. J.J. Brennan, ONR Technical Report, Contract No. N00014-82-C-0096, 1984.
13. J. Lankford, Ceram. Eng. Sci. Proc. (in press).
14. A.G. Evans and W.F. Adler, Acta met., 26 (1978) 725.
15. M.E. Kipp, D.E. Grady, and E.P. Chen, International Journal of Fracture, 16 [4] (1980) 471-478.

INVERSE STRAIN RATE EFFECTS AND MICROPLASTICITY
IN ZIRCONIA CRYSTALS

II.

James Lankford
Department of Materials Sciences
Southwest Research Institute
San Antonio, TX

Recently the compressive deformation of single crystal zirconia was compared with that of polycrystalline PSZ and TZP [1]. It was found that single crystal behavior was remarkably sensitive to orientation and temperature, and was mechanistically complex, involving transformation plasticity, ferroelastic domain switching, and dislocation activity. In particular, it was clear that dislocations were responsible for flow at intermediate temperatures (400-700°C), and they were inferred to accompany domain switching at room temperature. The purpose here is to describe the results of experiments aimed at exploring the effect of strain rate on the strength of zirconia crystals at 23°C.

Specimens were prepared, and compression tests performed, as described in detail elsewhere [1]. However, it should be noted that strain rates from 10^{-5}s^{-1} to 10^0s^{-1} were realized using a servo-controlled hydraulic machine, while a split Hopkinson pressure bar apparatus provided the capability of loading specimens to strain rates in excess of 10^3s^{-1} .

Two types of zirconia single crystal* were studied, i.e., one (20 w/o Y_2O_3) fully stabilized cubic, the other (5 w/o Y_2O_3) partially stabilized tetragonal. From a single parent crystal, cylindrical test specimens of 20Y-ZrO₂ were prepared with <123> axial orientations, and similarly from an

* Ceres Corp., Waltham, MA. The crystals are from the same batch studied by Ingel [2].

individual parent, specimens of 5Y-ZrO₂ were sectioned with either <123> or <100> orientations. The finite number of specimens which could be extricated from a given parent crystal limited the number of tests which could be run; all of the available specimens were tested.

The microstructure of the fully stabilized material is relatively simple, although certain details are unclear. In particular, the nominal crystal structure is cubic fluorite; the question concerns the status of the Y³⁺ ions within the lattice. It is assumed that the 20 w/o Y₂O₃ is distributed as a solid solution, unless significant clustering has occurred. However, X-ray diffraction of the crystals shows no evidence of a second phase [2], so that any clustering probably involves only a few atoms per cluster.

The microstructure of the partially stabilized material is complex, and not yet clearly defined. X-ray work by Ingel [2] indicated that both tetragonal and cubic phases were present, and his TEM work showed a dense (> 50 volume percent) distribution of tetragonal precipitates; these precipitates were coherent with the matrix, commonly twin-related with each other, and in a variety of forms, ranging from distorted ellipsoids to parallel-epipeds. They appeared to be around 400-1400 nm in length and 80-280 nm in width. On the other hand, Lankford, et al. [1], studied TEM foils taken from nominally equivalent crystals, and found that the microstructure consisted of three interlocking tetragonal variants of the metastable yttria-rich tetragonal (t') phase. These three variants coexist in equiaxed colonies on the order of 0.5 μm in size. Each colony consists of two variants with c-axes oriented 90 degrees from one another, forming alternating 80 nm bands separated by planar, twin-related {101} interfaces. Within the t' variants lie fine, coherent, yttria-poor, tetragonal (t) precipitates.

Results of testing these materials under uniaxial compressive loading are shown in Figure 1. It is evident that their strength (σ_c) declines with increasing strain rate ($\dot{\epsilon}$), irrespective of orientation (for 5Y-PSZ) and degree of phase stability (for the <123> orientation). Despite these differences, it is noteworthy that the slopes of the $\sigma_c - \dot{\epsilon}$ plots are reasonably uniform. Accuracy in determining the precise values of the slopes is constrained by the limited number of available test specimens.

The inverse relationship shown in Figure 1 is very unusual. Previously, it was found for a wide range of ceramics, including Al_2O_3 , SiC, and Si_3N_4 [3], as well as polycrystalline PSZ, TZP, and fully stabilized cubic zirconia [4], that σ_c increases slowly with $\dot{\epsilon}$. In particular, it was shown that

$$\sigma_c \propto \dot{\epsilon}^{1/(1+n)} \quad (1)$$

where n is the stress intensity exponent determined in a subcritical crack velocity (V-K) experiment. The rise in compressive strength with strain rate is thus thought to derive from the suppression of thermally activated subcritical microcrack growth. The latter microcracks nucleate athermally via brittle microfracture.

In the case of the zirconia crystals, something beneficial to their strength obviously is being suppressed with increasing strain rate. Since the same subcritical crack growth mechanism (Equation 1) should obtain for zirconia crystals, it would appear reasonable to try to determine whether some thermally activated stress relaxation process might be responsible for more difficult microcrack nucleation at lower strain rates. Accordingly, two fully

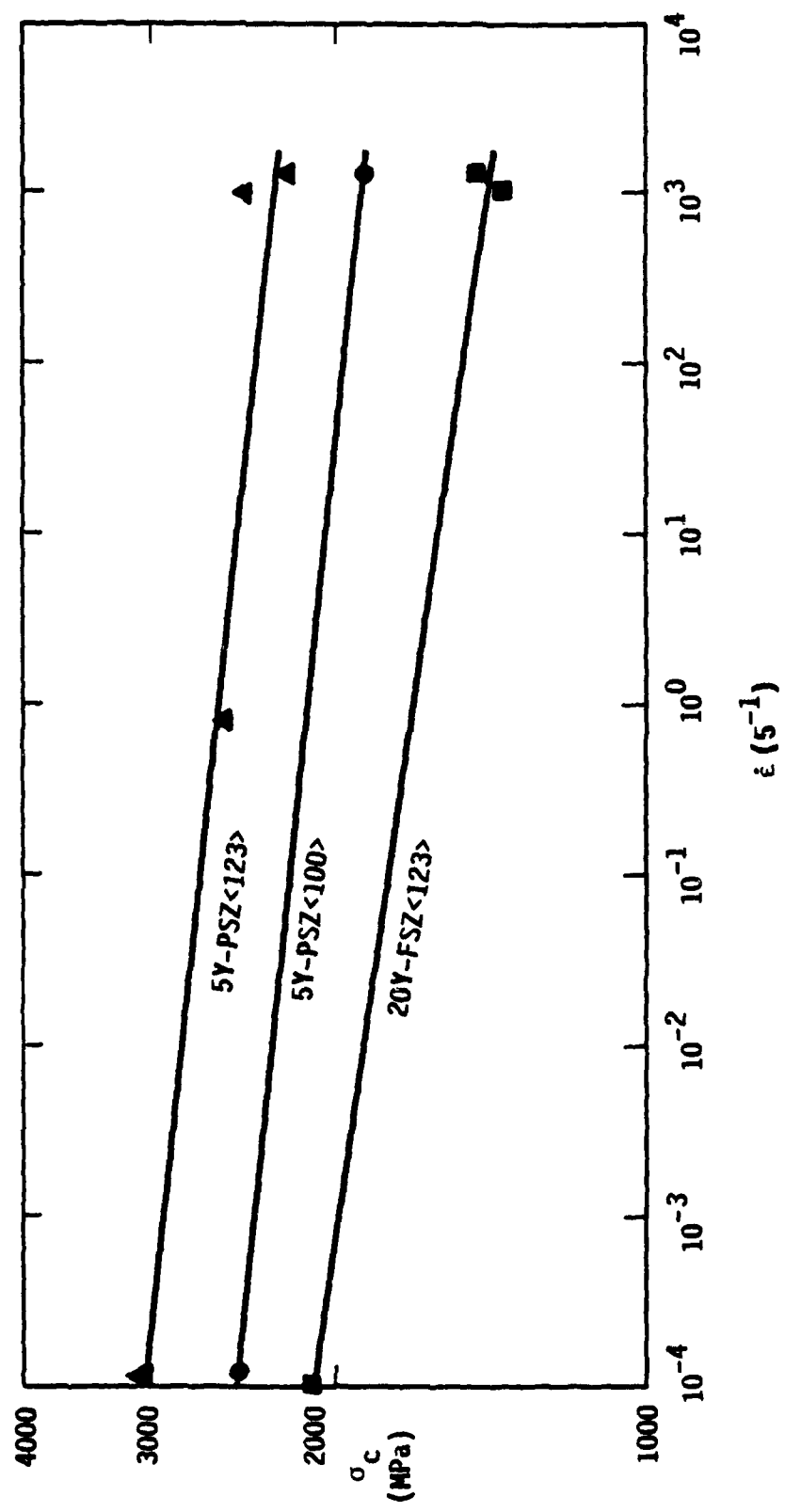


Figure 1. Compressive Strength Versus Strain Rate for Zirconia Single Crystals.

stabilized single crystals,* as well as a polycrystalline Al_2O_3 specimen, were mounted with strain gages paired in opposition to eliminate any nonlinearity caused by bending. Microstrain tests were performed by loading the specimens to a relatively high stress level, followed by unloading.

As shown in Figure 2a, the result expected for a classical brittle material (Al_2O_3) is as observed, i.e., the load-unload line is perfectly linear elastic. For the zirconia, on the other hand (Figure 2b), the behavior is more reminiscent of a classic metal; compare the inset, which shows the microstrain results of Rosenfield and Averbach [5] for polycrystalline copper. Both materials exhibit a plastic microyield point and microstrain hardening, followed upon unloading by anelastic recovery (caused by microcreep) and subsequent elastic unloading, and finally, reverse plastic flow as zero load is approached. The net irreversible plastic deformation is on the order of 650×10^{-6} . Since fully stabilized zirconia cannot transform, the observed behavior can only be attributed to dislocation activity. It is interesting to compare the relative stress amplitudes required to generate these qualitatively similar results in such dissimilar materials, i.e., the ratio of their yield strengths is approximately 40. Thus, σ_y for the ZrO_2 is equal to $-E/100$, while for the Cu, $\sigma_y = \frac{E}{5000}$.

Based on the zirconia crystal microstructure, it is likely that the yield point represents dislocation breakaway from pinning solute atoms (or clusters composed of a few atoms). An estimate of the required stress may be obtained by applying the low homologous temperature solution hardening relationship derived by Friedel [6], according to which

* Unfortunately, no further 5Y-ZrO₂ specimens were available. It is an explicit assumption here that their microstrain behavior would be qualitatively similar to that of the 20Y-ZrO₂ crystals.

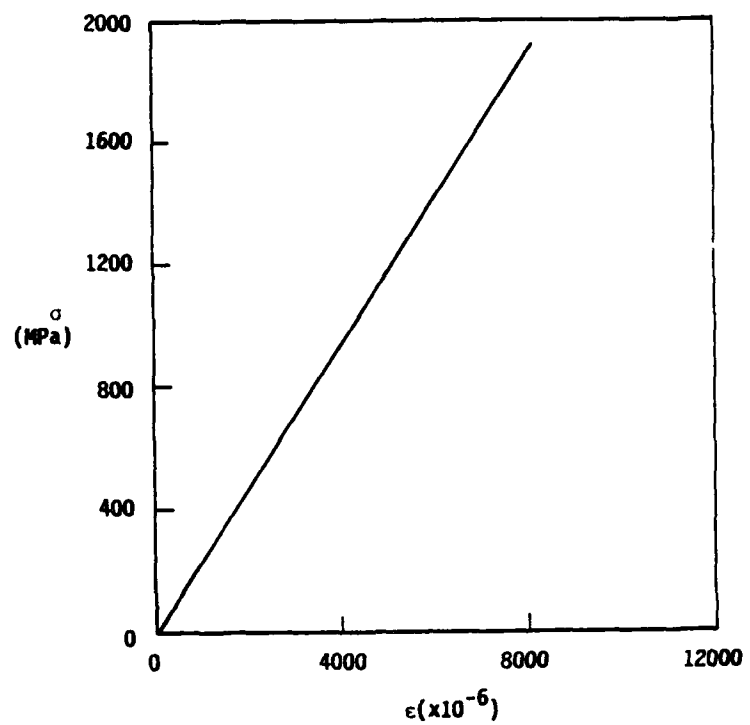
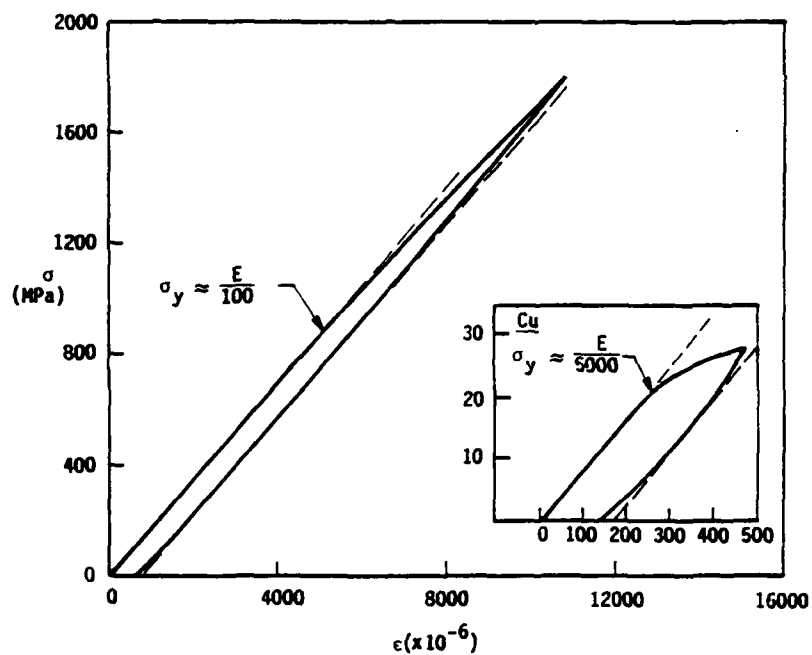
(a) Al_2O_3 (b) 20Y-ZrO₂ (inset shows data for polycrystalline Cu[5])

Figure 2. Stress-Microstrain During Compressive Load-Unload

$$\sigma_y \approx \frac{\mu n c}{4} \quad (2)$$

in which μ is the shear modulus, n is the elastic misfit parameter representing the difference in size between solute and solvent atoms, and c is the solute atomic concentration. For the 20 w/o - ZrO₂, $\mu = 130$ GPa, n is about 0.25 (based on the size difference between Y³⁺ and Zr⁴⁺), and $c = 0.074$ a/o. This model only accounts for elastic interactions between solute atoms and dislocations, it does not include stress relaxation due to charge compensating oxygen vacancies, or solute site-dislocation interactions due to valency effects. The latter increases the hardening when the valency of the solute atoms differs from that of the solvent [7]. Nevertheless, Equation 2 in the present instance predicts a yield stress of approximately 600 MPa, reasonably consistent with the measured value (Figure 2) of 860 MPa. Dominguez-Rodriguez, et al. [8], used a similar argument to explain a compressive plastic yielding in a series of similar fully stabilized zirconia crystals tested at 1400°C. In this case case, the high homologous temperature version of the dislocation-solute pinning analysis by Friedel [6] also predicted a yield strength in reasonable agreement with experiment.

In light of these results, it is suggested that the strain rate dependence shown in Figure 1 has a common origin in all three cases: as strain rate increases, microplastic relaxation of local internal stresses is inhibited, and must be replaced by microcracking. This concept is in accord with experiments in which the dynamic hardness of monolithic ceramics has been assessed. Several studies have shown that with increasing strain rate, hardness (H) increases dramatically [9-11]. This has been interpreted as a consequence of diminished thermally-activated dislocation activity. Moreover, the increased hardness (higher yield strength) at higher strain rates has been

correlated with more extensive microfracture [11], in accord with the proposed scenario for compressive loading.

It should be noted that the hardness derived yield stress does not translate directly to the microstrain yield stress. The former is given approximately by [10]

$$Y \approx \frac{H}{3} \quad (3)$$

and represents the yield laws for activation of the constrained multiple slip systems required for accommodation of a hardness indentation. Since H for the present 20Y-ZrO₂ is 15.3 GPa, Y ≈ 5100 MPa. Not surprisingly, this is well in excess of the 860 MPa required to yield the single most highly favored uniaxial compressive slip system. On the other hand, it is perfectly reasonable that both situations should scale in terms of their dependence upon strain rate.

ACKNOWLEDGMENTS

The support of the Office of Naval Research under Contract No. N00014-84-C-0213 is gratefully acknowledged. Thanks are expressed to A. Nicholls for his careful experimental work.

REFERENCES

1. J. Lankford, L. Rabenberg, and R. A. Page, J. Mat. Sci. (in press).
2. R. P. Ingel, "Structure-Mechanical Property Relationships for Single Crystal Yttrium Oxide Stabilized Zirconium Oxide," Ph.D. Thesis, The Catholic University of America (1982).
3. J. Lankford, in "Fracture Mechanics of Ceramics," Vol. 5, edited by R. C. Bradt, A. G. Evans, D.P.H. Hasselman, and F. F. Lange (Plenum Press, N.Y., 1983) p. 625.
4. J. Lankford, in "Advances in Structural Ceramics," Vol. 78, edited by P. F. Becher, M. V. Swain, and S. Somiya (Materials Research Society, Boston, 1987) p. 61.
5. A. R. Rosenfield and B. L. Averbach, Acta Met., 10 (1962) 71.
6. J. Friedel, "Dislocations" (Pergamon Press, London, 1964) p. 381.

7. A. H. Cottrell, "Dislocations and Plastic Flow in Crystals" (Clarendon Press, Oxford, 1963) p. 132.
8. A. Dominguez-Rodriguez, K.P.D. Lagerlof, and A. H. Heuer, J. Am. Ceram. Soc., 69 (1986) 281.
9. C. J. Fairbanks, R. S. Polvani, S. M. Wiederhorn, B. J. Hockey, and B. R. Lawn, J. Mat. Sci. Lttrs., 1 (1982) 391.
10. M. M. Chaudhri, J. K. Wells, and A. Stephens, Phil. Mag. A, 43 (1981) 643.
11. D. B. Marshall, A. G. Evans, and Z. Nisenholz, J. Am. Ceram. Soc., 66 (1983) 580.